

# AES 670 Final Project

Mitchell Dodson

March 26, 2023

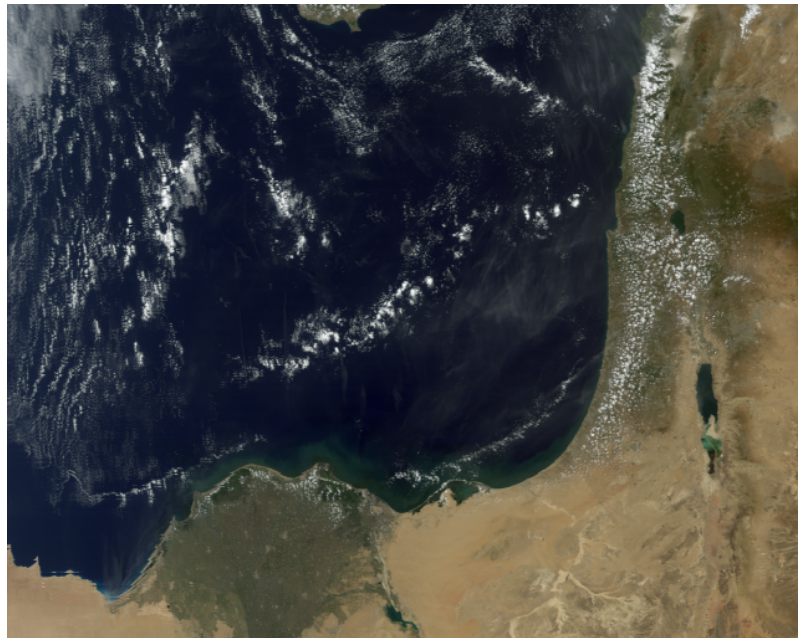


Figure 1: MODIS Truecolor image of my chosen region.

## 1 Abstract

In this project I perform K-means and maximum-likelihood pixel classification and subsequent analysis of MODIS L1b data in a region including the Southeast Mediterranean, the Nile River delta, and The Levant. The surface types I focus on are (1) ice clouds, (2) water clouds, (3) vegetation, (4) surface water, and (5) arid ground, though several other surface types were identified by classification. Correlation statistics and spectral analyses of surface classes are provided for each classification result. I will also use this report as documentation for the Python package I'm developing, as outlined in section 2.

## 2 Code comment

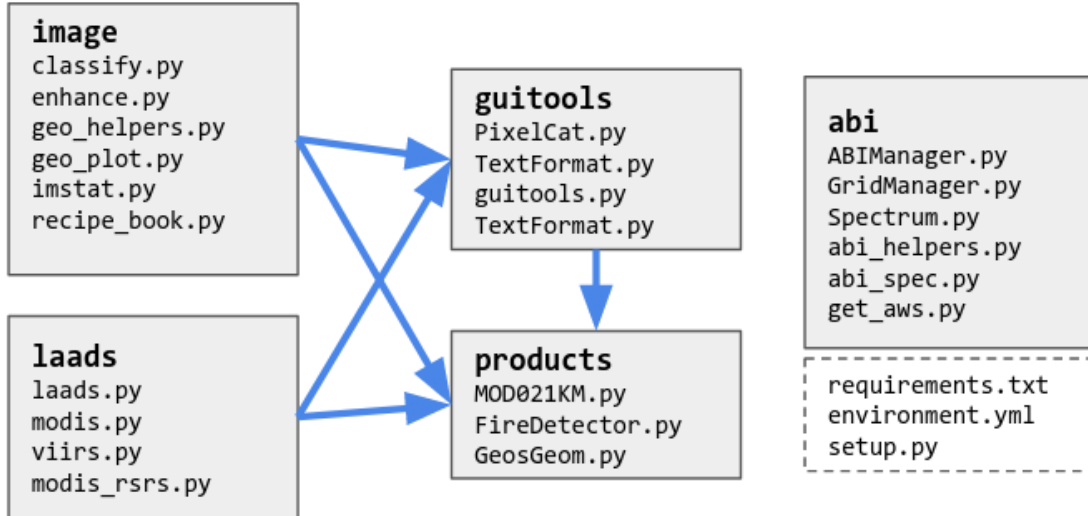


Figure 2: Module layout and dependency graph for my Python package for satellite data acquisition and analysis. The package is organized into modules containing generalized methods for a variety of tasks, as well as several classes for higher-level analysis. In accordance with Python naming convention, class files are capitalized and modules containing only methods are lowercase. My repository can be installed and imported like any other Python package, and is available on GitHub at <https://github.com/Mitchell-D/aes670hw2/>

One of my major goals for graduate school is to collect code I write for classes and research into a reusable package of software tools with a common architecture and a minimal number of dependencies, which I ultimately want to develop into an ongoing open-source software project. This class has enabled me to make significant headway on my goal, so this report will serve as both a surface analysis of my region and a demonstration of my software. Figure 2 shows the layout of my package, which is currently called `aes670hw2` (subject to renaming soon). The package and its dependencies can be installed manually with `pip install /path/to/aes670hw2`, or with `conda-forge` using the included `environment.yml` file. Any of the sub-modules can be imported directly from the package, for example `from aes670hw2 import enhance as enh`.

Software development is a balancing act between usability and re-usability. “Low-level” operations like N-dimensional histogram matching must be complicated enough to be useful to specialized tasks without the need for extra infrastructure code, and “high-level” methods like getting user input at runtime with a live-rendered RGB must be general enough to be used for a variety of data circumstances. As such, I’m keeping a wide range potential future use cases in mind for each every module, and attempting to stratify the methods within each module into a reusable collection of sub-tasks. For instance, `enhance.histogram_match` is a relatively high-level method that takes two equally-shaped 2d or 3d arrays and histogram-matches the first two axes of the first array to the first two axes of the second array in a provided number of bins. This method is only 19 lines long since it subsequently depends on `enhance.get_cumulative_hist`, `enhance.get_pixel_counts`, `enhance.norm_to_uint`, and other sub-tasks that are reusable for a wide variety of other purposes.

I have a long list of future plans for this project, which include developing API wrappers for data sources other than the LAADS DAAC and NOAA AWS buckets, adapting the `products.MOD021KM` class design to support any gridded dataset, and an asynchronous process queue to enable multiple simultaneous OpenCV2 windows. My codebase currently exceeds 7,500 lines of Python, which includes detailed internal documentation for every method. The following tables provide an overview of each module's purpose.

Module	Purpose
<code>products</code>	The <code>products</code> module contains three classes: <code>FireDetector.py</code> , <code>GeosGeom.py</code> , and <code>MOD021KM.py</code> . The first is a relatively simple class that executes the fire detection algorithm outlined in (Flasse & Ceccato, 1996) [1] with optional custom thresholds, and which only depends on numpy. The second is also a fairly simple but highly generalized class that generates surface latitude/longitude and pixel/sun/sensor trigonometry arrays from basic sun/satellite geometry information for any geostationary satellite. The third, <code>MOD021KM.py</code> , is however a very abstract class that provides a wide variety of methods for interfacing with and analyzing MODIS L1b data in the MOD021KM or MYD021KM formats. The class includes static methods for finding, downloading, parsing, calculating, and subsetting a user-provided set of L1b MODIS reflectance and brightness temperature bands to a geographic range. Since MOD021KM objects can be easily created from a L1b HDF, instances of the MOD021KM class are built on and enforce the principles that the underlying band data they are initialized with cannot change, that all contained datasets have an identical shape, and that any band composite recipe can be expressed as a directed tree graph of other composite recipes it depends on, all of which must ultimately terminate with raw band data as a “leaf node” argument. This enables the object to repeatably dynamically evaluate a hierarchy of recipe dependencies at runtime. For example, the user may provide the MOD021KM object a <code>guitools.Recipe</code> object with an arbitrary function (ie histogram equalization/matching, an analytic function, a 5-band composite), a string label, and a list of band or recipe labels corresponding to the function’s arguments. By referencing the label, the new Recipe can be enhanced, histogram-analyzed, rendered as an RGB, or used for threshold selection, classification, fourier analysis, etc. All of these operations can be accessed by calling a single respective method of the MOD021KM instance. The MOD021KM object also contains wrappers on many other methods for GUI selection and enhancement, K-means and migrating means classification, data mask creation/manipulation/comparison, etc, which will be used often throughout this report.
<code>abi</code>	The <code>abi</code> module is mostly adapted from one of my old codebases, and isn’t integrated with the rest of the package. It contains methods for querying the NOAA AWS Bucket for GOES East and GOES West ABI and GLM data ( <code>get_aws.py</code> ), subsetting, projecting, and aligning geolocated arrays ( <code>abi_helpers.py</code> and <code>GridManager.py</code> ), and for rendering animations and performing a variety of analyses on time series of ABI data ( <code>ABIManager.py</code> ).

Module	Purpose
image	The <code>image</code> module contains sub-modules with methods for performing enhancement and other pixelwise operations on general 2d and 3d arrays ( <code>enhance.py</code> ), plotting continuous and discrete 1d, 2d, and 3d data in a variety of formats with a common configuration format ( <code>geo_plot.py</code> ), manipulating and interpolating 2d and 3d arrays in multiple coordinate systems ( <code>geo_helpers.py</code> ), performing histogram analysis, equalization, and matching on arbitrary 2d and 3d arrays ( <code>enhance.py</code> ), applying arbitrary convolutional kernels to arrays with several hardcoded options, running my fast-fourier implementation and applying user-defined frequency masks ( <code>enhance.py</code> ), and contains a variety of hardcoded RGB recipes ( <code>recipe_book.py</code> ). This module has no dependencies that aren't installed by default in Python <code>wheel</code> .
laads	The <code>laads</code> module currently consists of 3 main sub-modules: <code>laads.py</code> , <code>viirs.py</code> , and <code>modis.py</code> . The <code>laads.py</code> sub-module contains a collection of abstract methods for querying the Earth Observing System's LAADS DAAC archive's REST API, enabling the user to retrieve information about, search for, and download any available product with optional geographic and time constraints. The <code>viirs.py</code> and <code>modis.py</code> sub-modules use <code>laads.py</code> to search for user-specified L1b or L2 swaths at any resolution, and provide methods for parsing their respective data files into a common format consisting minimally of a tuple of requested band arrays, and a list of dictionaries corresponding to each band with meta-information such as conversion coefficients, units, and center wavelengths. These methods also optionally provide coordinate reference, sun/satellite geometry, and terrain information if available.
guitools	The <code>guitools</code> module contains the self-titled sub-module <code>guitools.py</code> as well as two specialized classes <code>PixelCat.py</code> and <code>TextFormat.py</code> . The main dependency of this module is the Python wrapper for OpenCV2, which <code>guitools.py</code> uses to provide functions to get user input with GUI interfaces and to perform a variety of RGB rendering operations. The sub-module contains GUI methods with interactive windows prompting the user to select a group of pixels in an image, select a rectangular or circular region of an image, or select a scalar value for the image. The latter method re-renders the image in the window using an arbitrary user-defined function of the array and a scalar variable. This function can be defined to let the user interactively choose contrast, gamma, histogram mean, and value thresholds for an arbitrary scalar array. <code>guitools.py</code> also contains lower-level methods for rendering a scalar array as an RGB using linear functions of hue, saturation, and value, returning a PNG as a numpy array, generating an array of unique colors, and getting an RGB array with normally-distributed color histograms according to user-defined means and standard deviations for each channel. The <code>PixelCat</code> class is a high-level class offering wrappers on GUI utilities for performing fourier analysis on, enhancing, and selecting pixels from arbitrary RGB arrays, and the <code>TextFormat</code> class colors and formats strings using ANSI escape codes for pretty terminal printing.

### 3 Data and domain of analysis

---

**NOTE:** In order to prevent confusion between class and object methods, I will refer to static class methods with the notation `MOD021KM.static_method`, and methods that must be called on an instance of the object with the notation `subgrid.object_method`, where `subgrid` is presumed to be a `MOD021KM` object with all the needed bands loaded. Instances may be initialized like `subgrid = MOD021KM.from_hdf(11b_hdf, 11b_bands)` or `subgrid = MOD021KM.from_pkl(pkl_path)`.

### 3 Data and domain of analysis

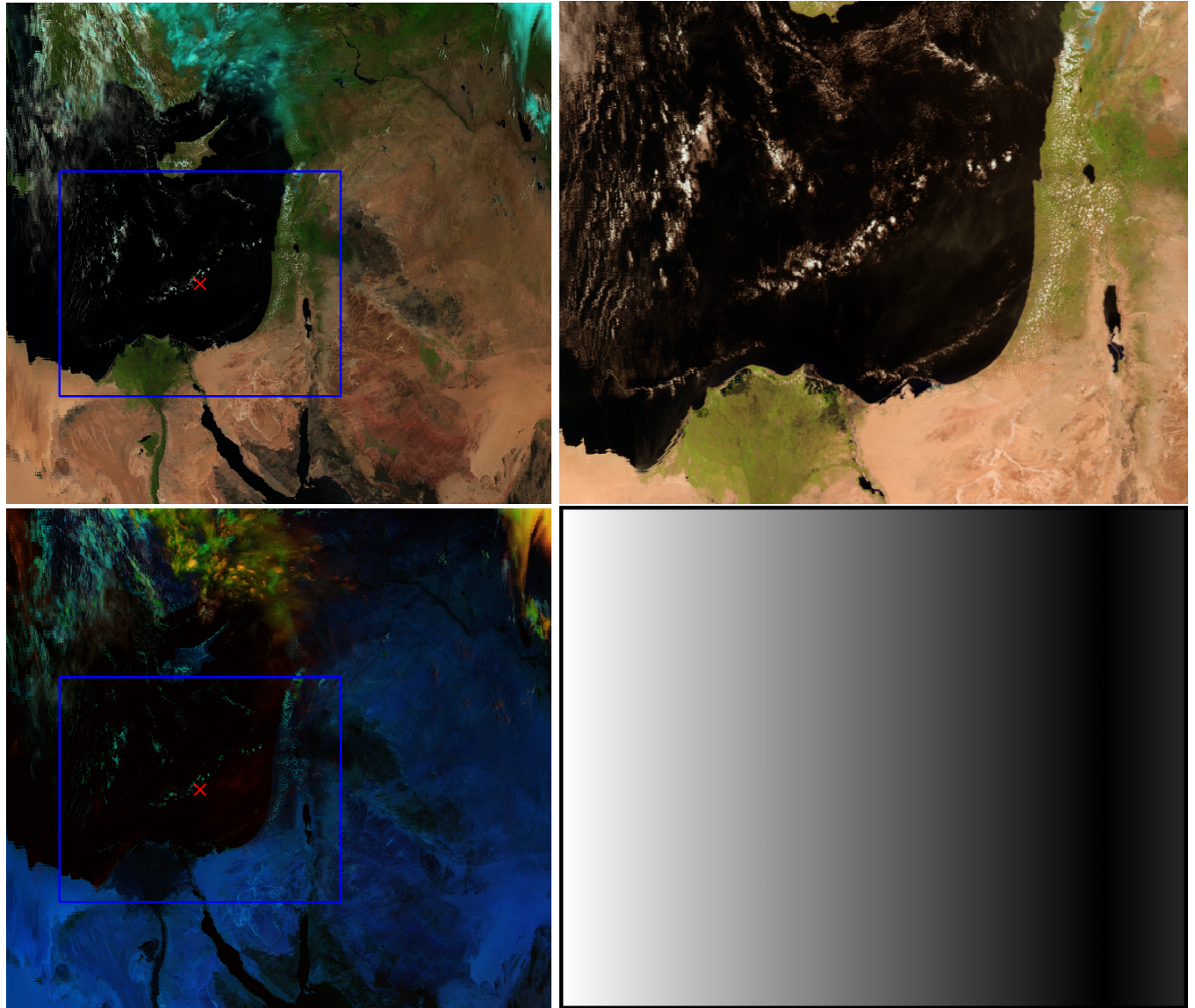


Figure 3: Top: Natural-color RGBs of a wide view of the location of my region and a focused view of the subgrid I used for analysis, which features the East Mediterranean, the Southern tip of Cyprus, and the Nile River delta on the left, with the Sinai Peninsula and the Levant on the Right. Bottom: Daytime cloud phase RGB composite of a broad view of my region, and a scalar mapping of the viewing zenith angle within my subgrid, which ranges from  $0^\circ$  (NADIR; black) to  $52^\circ$  (white) from vertical.

### 3 Data and domain of analysis

---

Figure 3 provides context on the region that I selected, which is centered on 32.41° East, 32.99° North and covers a total surface area of 528,689.3km. The MODIS L1b granule that includes my image was captured by the Terra platform on May 10, 2019 at 0829z, or 10:29am local time in Egypt. I downloaded the L1b data with `MOD021KM.download_granule`, providing the desired platform, target time, and geographic range of my domain, then initialized a MOD021KM object with the HDF file and a list of all the bands in Table 2 using `subgrid = MOD021KM.from_hdf`.

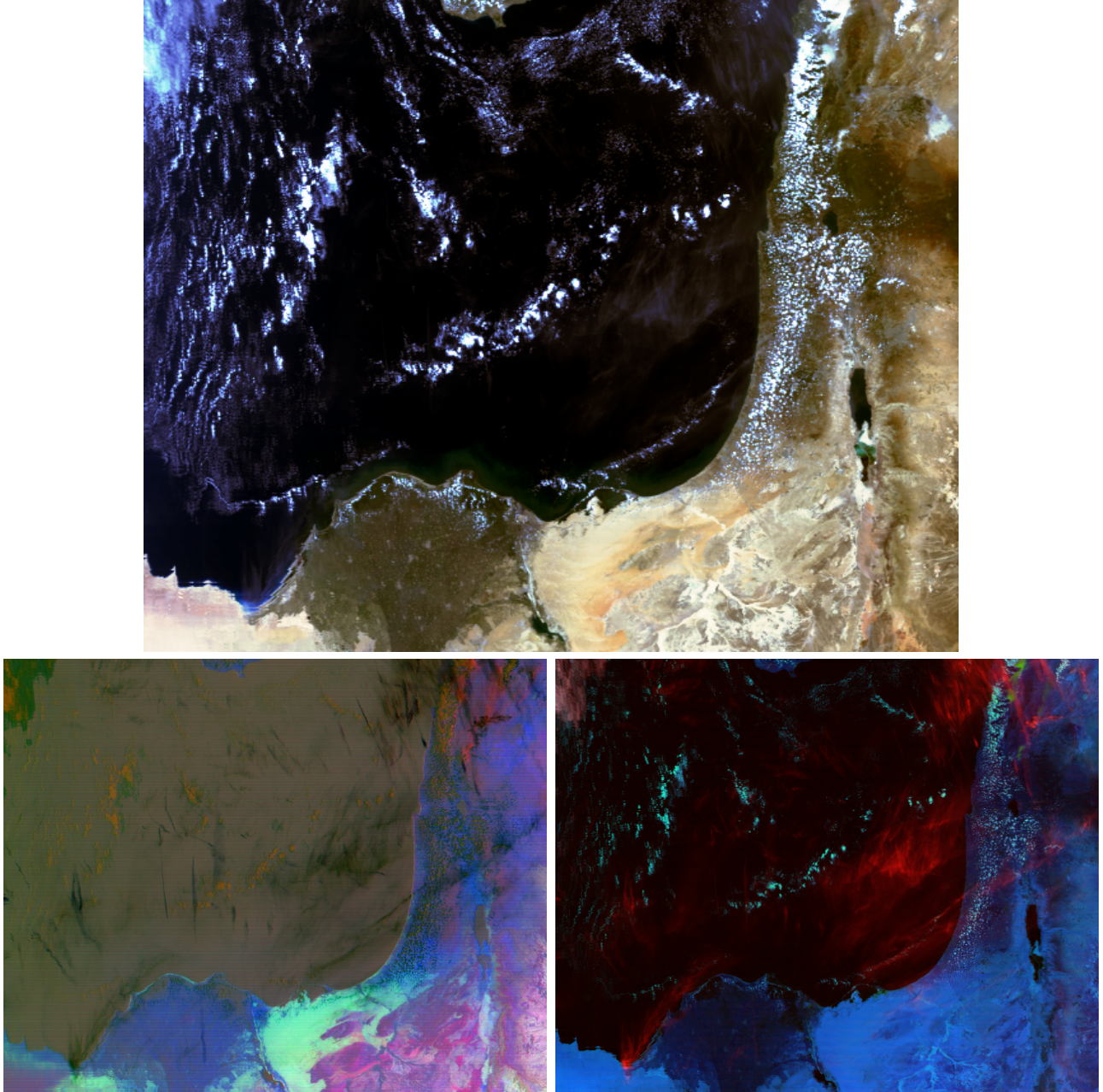


Figure 4: Top: histogram-equalized and gamma-enhanced true color RGB. Bottom: gamma-enhanced dust RGB [2] and daytime cloud-phase RGB [3]. Each of these recipes are loaded by default in `MOD021KM` objects with the labels “CUSTOMeq,” “DUST,” and “DCP.” They were generated with enhancement values manually chosen using the GUI launched by `subgrid.get_rgb("DUST", choose_gamma=True)` for each RGB label.

### 3 Data and domain of analysis

---

Dust RGB channels	Description
RED=norm( $12 - 11\mu m$ )	Cloud and dust optical thickness. Optically thick clouds and clear-sky land surfaces have values near zero, which are normalized to become bright since channel difference values generally range from $-5^{\circ}C$ to $1^{\circ}C$ . Low values indicate more attenuation by water vapor than $12\mu m$ .
GREEN=norm( $11 - 8.6\mu m$ )	Cloud particle phase and land surface emissivity. The 8.6. Water-phase clouds and surfaces with low emissivity have high values. Atmospheric columns with more water vapor absorption will also be tinted green.
BLUE=norm( $11\mu m$ )	LWIR window for cloud-top and land temperature.
Day-cloud RGB channels	Description
RED=norm( $1.38\mu m$ )	Cirrus cloud detection due to strong water vapor attenuation at mid and low layers
GREEN=norm( $.64\mu m$ )	Visible band for cloud optical thickness
BLUE=norm( $1.64\mu m$ )	Cloud-phase distinction; Water droplets are reflective, but ice particles strongly absorb.

Table 1: Recipes for false-color RGBs in Figure 4. Note that the sources for these RGB recipes limit data to certain ranges and apply specific gamma enhancements. Those values aren't included here since they can be selected to suit a task at runtime with `subgrid.data("label", choose_contrast=True, choose_gamma=True)`.

The histogram-equalized true color RGB in Figure 4 clearly shows the transition between the barren sandy desert surrounding the Nile Delta and the exposed rock and scrub of the Sinai peninsula, which is corroborated by corresponding light blue/green and magenta surfaces in the dust RGB. The GREEN band of the dust RGB recipe is the  $11 - 8.6\mu m$  LWIR channel difference, which is highly sensitive to the emissivity properties of barren land surfaces [4]. Bare stone and soil generally have an emissivity  $\epsilon \approx .92$ , and sand has an emissivity  $\epsilon \approx .89$ , which causes the brightness temperature of sand to appear artificially cool in the  $8.6\mu m$  band. This inflates the channel difference over sandy surfaces, hence the green hue of that region in the dust RGB.

The  $11 - 8.6\mu m$  channel difference in the dust GREEN channel also contributes more heavily to water-phase clouds than ice-phase clouds due to the much higher emissivity of ice than water, which explains the green tint of low-level water clouds in the RGB. The dust RGB's RED band is the  $12 - 11\mu m$  channel difference, which takes advantage of the additional water vapor attenuation in the  $12\mu m$  band to quantify cloud optical depth, as the ratio of surface emissions absorbed at  $12\mu m$  to emissions absorbed at  $11\mu m$  slightly increases with the amount of water vapor in the atmospheric column. Thus, the tan/orange clouds in the RGB correspond to optically-thick water and mixed-phase clouds, and the dark green pixels correspond to optically-thin and sub-pixel water clouds. The BLUE channel of the dust RGB is simply the  $11\mu m$  LWIR window channel, so cirrus clouds are black due to their high emissivity, low optical depth and cold temperature.

The daytime cloud-phase RGB assigns the  $1.38\mu m$  cirrus band to RED, the  $6.4\mu m$  red band to GREEN, and the  $1.64\mu m$  cloud-phase band to BLUE. Since water absorbs

### 3 Data and domain of analysis

---

very strongly in the NIR range, there is stark contrast between the Mediterranean sea surface, low-level and sub-pixel water clouds, and high-level cirrus clouds. The red streaks throughout the center of the image suggest pervasive thin cirrus contamination over the sea and Israel. Compared to the large-scale daytime cloud phase RGB in Figure 3, it's clear that these cirrus are very optically thin, which poses challenges in later analysis.

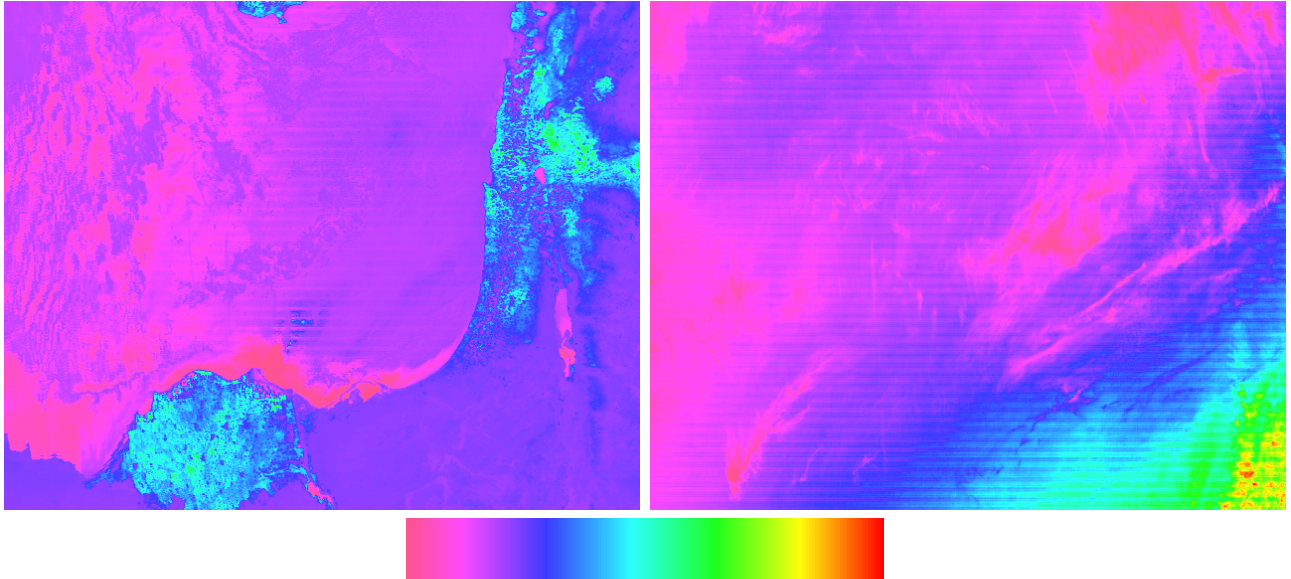


Figure 5: Left: gamma-enhanced NDVI heatmap (using  $.86\mu m$  NIR and  $.64\mu m$  RED bands). Right: gamma-enhanced band 28 ( $7.3\mu m$ ) brightness temperature heatmap. Both conform to the color bar with low values in magenta and high values in red. These are generated with `gui.tools.scal_to_rgb`, for example: `gui.tools.scal_to_rgb(subgrid.data("ndvi",choose_gamma=True))`. Hue, saturation, and value ranges for the RGB-mapped scalar array can be optionally provided.

The left image in Figure 5 shows a heatmap of vegetation on the banks of the Mediterranean, which captures the arid climate of the Sinai peninsula, the sparse vegetation of the Jordanian highlands, and the highly-vegetated Nile Delta and Levant regions, as well as the southern tip of Cyprus. The right image shows the  $7.175 - 7.475\mu m$  mid-level water vapor band, which features cold brightness temperatures indicating a steep gradient of vapor content increasing to the Northwest over the sea. Water vapor is especially concentrated along the West edge of the region, which is further occluded by sub-pixel clouds and panoramic distortion as the true color RGB in Figure 4 and viewing zenith angle render in Figure 3 suggest.

Both of the images in Figure 5 also show the effects of data striping, perhaps due to faulty cross-calibration of data from adjacent scan mirrors. Unfortunately bands 2, 5, 6, 7, 21, 26, 27, 28, and 33 were all somewhat affected by the striping. Although this poses some challenges in classification, enough bands were salvagable or intact to achieve reasonable results. Table 2 shows the range of bands I chose for initial analysis. The 11 bands I ultimately selected for classification tasks after experimenting with K-means in Section 6 are marked with an asterisk in the table.

### 3 Data and domain of analysis

---

<b>Band</b>	<b><math>\lambda (\mu m)</math></b>	<b>Justification</b>
03*	.459 – .479	Blue band: True color BLUE; sensitive to aerosols.
10	.483 – .493	Teal/blue: ocean color and general reflectivity.
04*	.545 – .565	Green: Vegetation, NDSI, and true color GREEN.
01*	.620 – .670	Near-red: land surface properties, true color RED.
02*	.841 – .876	NDWI for surface water, and NDVI due to the high reflectance of chlorophyll in the near-infrared range.
16	.862 – .877	Ocean color and aerosol distinction
19*	.916 – .965	Partial H <sub>2</sub> O absorption, for column moisture estimates.
05*	1.230 – 1.250	Cloud/aerosol optical depth and land surface properties.
26*	1.360 – 1.390	Steep H <sub>2</sub> O absorption curve for high cloud reflectance.
06	1.628 – 1.652	Snow/ice band: indices of refraction differ between ice and liquid-phase water. Water clouds are reflective and ice clouds strongly absorb.
07	2.106 – 2.155	Cloud and aerosol particle size band: small particles are similar in size to 2.2 $\mu m$ , so they are readily reflected via Mie scattering. Large particles absorb incident light [5].
20*	3.660 – 3.840	SWIR “Magic band”: solar reflectance as well as infrared emissions. Useful for a variety of derived products, especially for fire detection.
21	3.929 – 3.989	Infrared-biased narrow SWIR for cloud and land surface temperature. Spans the edge of a CO <sub>2</sub> absorption line.
27	6.535 – 6.895	High infrared cloud features due to very strong H <sub>2</sub> O absorption.
28*	7.175 – 7.475	Mid-level infrared cloud properties due to moderate attenuation by atmospheric water vapor.
29*	8.400 – 8.700	Infrared cloud phase and land features, as well as atmospheric column water content from weak vapor absorption. Sensitive to the emissivity of surfaces.
31*	10.780 – 11.280	Clean long-wave window band: very little atmospheric absorption, so the actual temperature of surfaces can be estimated with knowledge of their emissivity.
32	11.770 – 12.270	LWIR window: observed temperatures are slightly sensitive to artificial cooling depending on the altitude of the pixel surface.
33	14.085 – 14.385	Dirty LWIR: much stronger attenuation by water vapor makes it easy to characterize column vapor content.

\* Starred bands indicate the subset chosen for use in K-means and maximum-likelihood classification. All bands were used for analysis.

Table 2: Band number, spectral response range, and purpose of every MODIS band I used for analysis.

## 4 My custom RGB

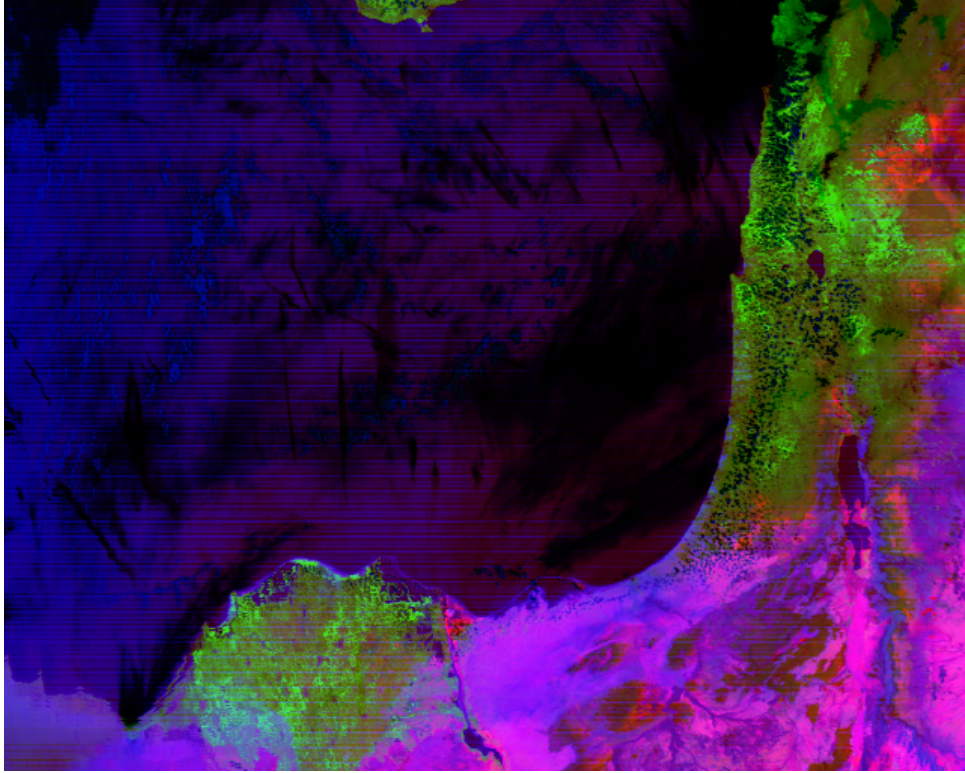


Figure 6: My custom RGB, enhanced to reveal land surface temperature and emissivity, vegetation density, atmospheric vapor content, and to mask thin clouds.

Custom RGB channels	Description
RED  RED <code>gamma(hist(norm(R)))</code> R= $T_B(11\mu m)$	LWIR window band, histogram-matched to a normal distribution with $\mu = .5$ and $\sigma = .2$ . Saturates cold temperatures to indicate land and sea surface temperature, distinguish land from clouds, and enhance land features.
GREEN  GREEN <code>gamma(hist(norm(G)))</code> G=NDVI $ _0^1$	Subsetted and normalized NDVI, histogram-matched to a normal distribution with $\mu = .3$ and $\sigma = .2$ . Saturates clouds and water near zero and stratifies the brightness histogram over high brightness values in the vegetation range.
BLUE  BLUE <code>gamma(hist(norm(B)))</code> B= $T_B(11\mu m) \div T_B(8.6\mu m)$	Normalized $11 \div 8.6\mu m$ band ratio, histogram-matched to a normal distribution with $\mu = .5$ and $\sigma = .3$ . Sensitive to land surface emissivity and atmospheric vapor content.

Table 3: Custom RGB recipe. Normal distribution values are selected to provide baseline histograms, which can be shifted with gamma enhancement to accentuate the features needed for a specific task.

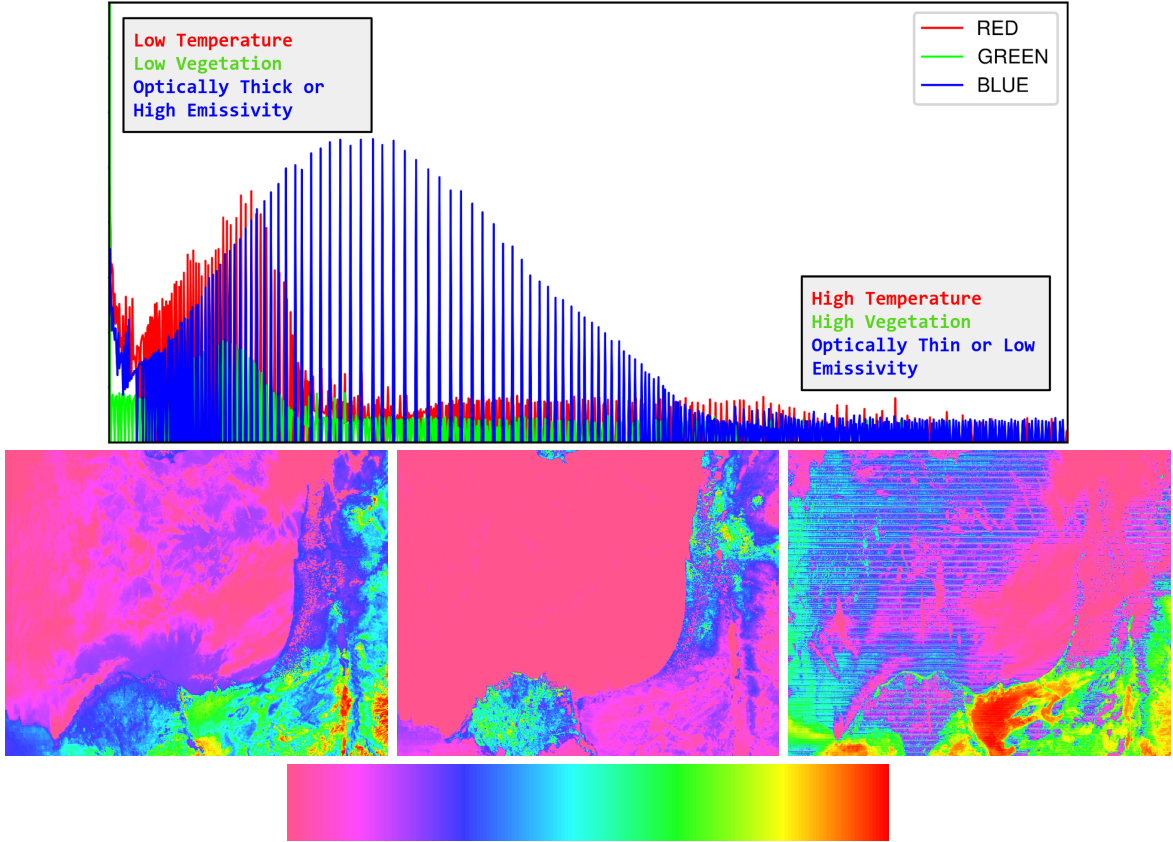


Figure 7: Normalized brightness frequency histogram, and heat map renders of each color component’s scalar array with a colorbar demonstrating the data distribution from minimum (magenta) to maximum (red).

In order to further investigate the features identified in Section 3, I developed an RGB sensitive to vegetation, precipitable water vapor (PWV), land surface and cloud-top temperatures (LST, CTT), and land surface emissivity (LSE). As outlined in Table 3, the RED band is the longwave infrared window, which corresponds directly to LST and CTT, and serves as a reference point for BLUE channel values. The GREEN band is the NDVI with the  $.86\mu m$  and  $.64\mu m$  bands (1 and 2), with high and low values cropped to the  $[0, 1]$  range, then normalized, which saturates barren land, clouds, and water and enhances vegetation density. The BLUE band is the  $11 \div 8.6\mu m$  longwave infrared band ratio, the behavior of which is the most difficult to intuit since bright values correspond to different phenomena on land and in the atmosphere.

On one hand, in the atmosphere, the BLUE band ratio is large where  $8.6\mu m$  band brightness temperatures are suppressed by water vapor as discussed in Section 3. This is apparent at the edges of water clouds, in regions with sub-pixel clouds, and in regions with high PWV. Optically thick (and especially high-altitude) clouds have similar brightness temperatures in both bands, and as such have low ratio values. In clear-sky regions, on the other hand, the BLUE band ratio is dominantly sensitive to LSE. The inverse Planck function `modis.get_modis_data` uses to calculate brightness temperatures from infrared radiance implicitly assumes that the emissivity of incident surfaces is  $\epsilon = 1$ . Since the  $8.4 - 8.7\mu m$  band occupies a spectral range right on the steep low-wavelength edge of the  $T \approx 300K$  blackbody emission curve, it is more sensitive to error in this assumption. Thus low-emissivity surfaces like sand ( $\epsilon \approx .89$ ) appear brighter in the ratio than high-emissivity surfaces like vegetation ( $\epsilon \approx .94$ ).

Both of the phenomena influencing the BLUE band ratio are ultimately the consequence of changes in emissivity among surfaces, as atmospheric layers with a low optical depth equivalently have low emissivity. Nonetheless, my RGB's property that low LSE and high PWV both correlate with high BLUE brightness values can make interpretation challenging. For example in Figure 6, the sandy region Southwest of the Nile Delta appears artificially more blue than the similarly sandy region at the East edge of the delta due to the presence of PWV from the moist airmass seen in Figure 5.

I created the custom RGB featured in Figure 6 by adding new scalar recipes for each channel, for example: `subgrid.add_recipe("LWrat", (29, 31), lambda a,b: norm(b/a))`, then an RGB recipe with arguments for each channels using `subgrid.add_rgb_recipe`. Next, I called `guitools.get_normal_rgb` to generate an RGB array with the same shape as my data, which contains normally-distributed scalar values in each 2d channel corresponding to the means and standard deviations specified in Table 3, which are sampled in the [0, 1] range. Then I histogram-matched my custom RGB recipe to the normally-distributed RGB array with `subgrid.histogram_match`, adding the data array to my `subgrid` object with `subgrid.add_rgb_data("CUSTOMhist", rgb)`. Finally, I shifted the brightness histograms to distributions convenient for land-surface analysis by calling `subgrid.get_rgb("CUSTOMhist", choose_gamma=True)`.

Figures 6 and 7 are the results of executing this procedure for a single RGB. The spectral distribution in Figure 7 was generated by calling `subgrid.rgb_histogram_analysis` with the RGB's data label "CUSTOMhist". Each channel heatmap in the figure was generated by getting an RGB for each color by calling `guitools.scal_to_rgb` with custom HSV range parameters, then generating the images with `gui.plot.generate_raw_image`.

Low-density vegetation appears brown due to mid-brightness contributions from each channel since partially-vegetated land surfaces are generally warmer, have a lower NDVI, and have a lower total emissivity than heavily vegetated areas. The same logic applies to high and low-vegetation regions since NDVI strongly correlates with surface emissivity as outlined in (Van De Griend, 2007)[6]. After consulting a geographic atlas [7], I realized that the red regions in Jordan and Syria correspond very closely to the Sinai mountain ridge and the Judaean mountains. The geology of this region suggests that these areas mostly consist of exposed and fragmented limestone, which has an emissivity around  $\epsilon = .95$ . The surrounding pink and purple regions are dominantly loamy soil and exposed sandstone, which have emissivities around  $\epsilon = .92$  [7][8][9], hence the contribution from the BLUE channel.

The blue-tinted regions over the Mediterranean on the left of the Figure 6 demonstrate the PWV of the moist air mass over the Mediterranean, as discussed. Optically thick water and dense ice clouds appear black over land and water appear due to their high emissivity and low temperatures in the LWIR window band. The top right of the image features thin cirrus clouds over a vegetated surface, which appear blue/green due to their low emissivity and the diffusion of near-infrared reflectance from vegetation through the cloud. This is an additional example of the interpretation challenge mentioned previously.

## 5 Data thresholding

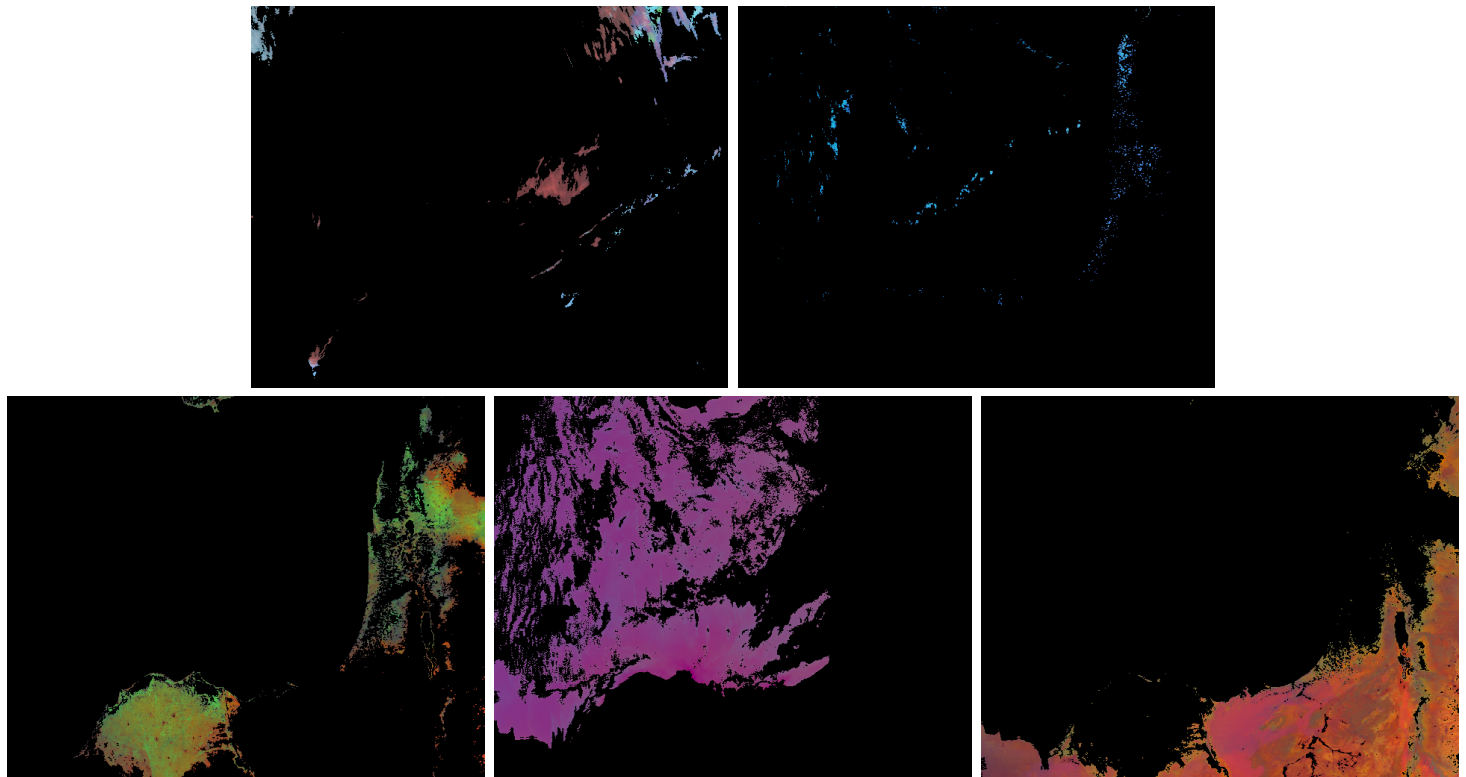


Figure 8: Masks selected by thresholding procedure. Top: ice cloud and water cloud surface classes. Bottom: vegetation, water, and arid surface classes. Unmasked data values are histogram-matched to the primary RGB used to isolate the class.

In order to isolate the 5 surface types I’m analyzing, I manually selected valid reflectance and brightness temperature ranges with `subgrid.get_mask` for a series of bands and RGB recipes. This method launches a GUI interface with a trackbar input form and an image that is rendered with a callback loop depending on the value of the input. For each channel of each RGB in my procedure, I used the trackbar to select a lower and upper bound for the mask. After data ranges for a surface class were determined, I histogram-matched the in-range values to the RGB that best accentuates the surface type using `subgrid.histogram_match`. Figure 8 shows the results, which rule out pixels that were out of bounds for any channel in any image used for thresholding the class.

Histogram-matched surface class masks are useful for interpretation because the histogram matching process spreads out brightness values of RGB channels with high variance for data values in the class. For example, the vegetation mask was histogram-matched to my custom RGB. There are a wide range of plant densities visible in this mask due to the variability in the RED (LWIR) and GREEN (NDVI) channels of my custom RGB. The water mask, which was also matched to my RGB, features a bright region just Northeast of the Nile Delta, which corresponds to warmer regions in the RED (LWIR) channel from a relative lack of sub-pixel clouds and atmospheric moisture, as suggested by the  $7.3\mu\text{m}$  channel rendering in Figure 5, and the relatively high temperature and low emissivity in this region indicated by Figure 7’s RED and BLUE channels.

## Thresholding methodology

1. The **ice cloud** class is selected with upper and lower bounds on each channel of the daytime cloud-phase RGB, which includes the  $1.38\mu m$  cirrus band for middle and low-cloud masking as well as the  $1.64\mu m$  cloud-phase band to rule out water clouds.
2. The **water cloud** mask is selected by masking ice clouds with the daytime cloud-phase RGB, and land surfaces with my custom RGB.
3. The **arid land** mask is selected using my custom RGB, which was specifically enhanced to accentuate land features and vegetation as discussed in Section 4.
4. The **vegetation** mask is also selected with my custom RGB, using a different gamma enhancement after histogram-matching which is selected manually to better expose vegetation. I used my own discretion to set boundaries where vegetation became too sparse.
5. The **water** class is the most difficult to isolate due to the abundance of PWV and sub-pixel clouds in my case. Optically thick clouds and most land are masked with my custom RGB, then coastlines are masked with the  $8.6 - 2.1\mu m$  NIR water index (NDWI). Finally, all prior masks are negated from the water mask.

	Ice Cloud	Water Cloud	Vegetation	Water	Arid
Pixel Count	10,094	2,227	36,614	96,730	68,922
Area ( $\text{km}^2$ )	14,426	3,221	48,431	181,319	85,435

Table 4: Area and quantity of thresholded pixel classes.

Table 4 shows the number of pixels and approximate surface area of each of the classes derived from thresholding. Areas were calculated for each surface type by passing the 2d boolean array returned by `subgrid.get_mask` to the `subgrid.area` method, which returns the sum of the surface areas of unmasked pixels by calculating the pixelwise panoramic distortion with the viewing zenith angle array (`subgrid.data("vza")`). This table makes clear that water and arid land dominate the region, followed by vegetated land surfaces.

Ice clouds and water clouds are under-represented because I intentionally chose restrictive thresholds for these classes. Clouds in general were difficult to threshold due to the scarcity of vapor bands uncorrupted by striping, the wide range of PWV values in my region, and the presence of mixed-phase clouds over the Mediterranean. For example, note the light blue mid-level water-phase clouds present on the right side of the ice cloud mask in Figure 8. These inhabit a region with low precipitable water vapor and a very thin cirrus layer, and as such weren't masked with a lower bound on LWIR brightness temperature or the  $1.37\mu m$  cirrus band. Since I will sub-sample my thresholded classes to use as training samples for maximum-likelihood classification, I wanted to leave as little ambiguity as possible in each class' spectral signature.

### Thresholded surface classes: spectral response and error

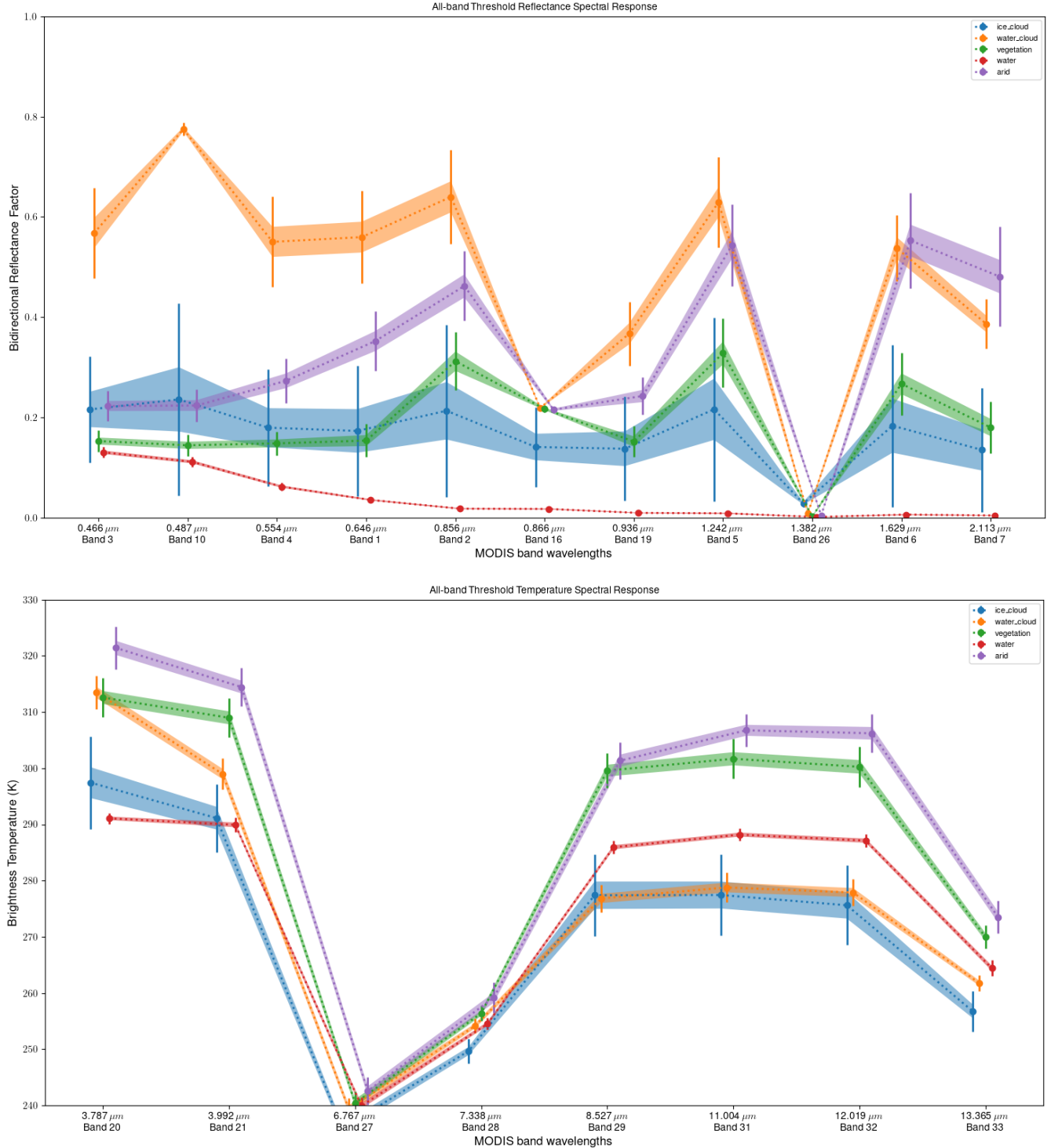


Figure 9: Reflective and thermal spectral response of each threshold-derived surface class. Each data point is the mean value of the class at that wavelength with  $1 - \sigma$  error bars and  $\frac{1}{3} - \sigma$  shaded regions.

$\lambda$	$\mu$	$\sigma$	Reflectance Covariance ( $\times 10^4$ )							
Ice Cloud										
0.466	0.216	0.105	111.3	118.5	125.2	138.0	88.5	135.7	0.5	
0.554	0.180	0.117	118.5	136.2	150.1	180.7	112.2	181.6	0.6	
0.646	0.173	0.130	125.2	150.1	169.8	211.0	129.4	215.2	0.6	
0.856	0.214	0.172	138.0	180.7	211.0	295.0	176.3	309.1	1.1	
0.936	0.138	0.104	88.5	112.2	129.4	176.3	107.7	184.0	0.9	
1.242	0.216	0.183	135.7	181.6	215.2	309.1	184.0	335.2	1.2	
1.382	0.029	0.008	0.5	0.6	0.6	1.1	0.9	1.2	0.6	
Water Cloud										
0.466	0.560	0.092	84.9	81.5	81.2	82.5	68.0	47.9	0.0	
0.554	0.640	0.093	81.5	86.7	75.1	78.8	76.1	54.3	0.9	
0.646	0.568	0.090	81.2	75.1	81.3	80.1	61.9	41.8	-0.6	
0.856	0.550	0.090	82.5	78.8	80.1	80.7	65.4	45.8	-0.1	
0.936	0.629	0.090	68.0	76.1	61.9	65.4	81.0	49.5	1.1	
1.242	0.367	0.063	47.9	54.3	41.8	45.8	49.5	40.2	1.7	
1.382	0.009	0.006	0.0	0.9	-0.6	-0.1	1.1	1.7	0.3	
Vegetation										
0.466	0.154	0.033	10.9	8.4	4.6	7.0	14.3	5.3	0.4	
0.554	0.312	0.058	8.4	33.5	4.4	7.2	36.5	15.0	0.1	
0.646	0.153	0.021	4.6	4.4	4.4	4.5	6.3	0.7	0.0	
0.856	0.149	0.024	7.0	7.2	4.5	5.6	10.5	3.1	0.1	
0.936	0.329	0.068	14.3	36.5	6.3	10.5	46.8	18.0	0.4	
1.242	0.152	0.031	5.3	15.0	0.7	3.1	18.0	9.6	0.4	
1.382	0.003	0.003	0.4	0.1	0.0	0.1	0.4	0.4	0.1	
Water										
0.466	0.036	0.005	0.2	0.1	0.3	0.3	0.1	0.1	0.0	
0.554	0.018	0.004	0.1	0.1	0.2	0.2	0.1	0.1	0.0	
0.646	0.131	0.010	0.3	0.2	1.1	0.5	0.1	0.0	-0.0	
0.856	0.062	0.007	0.3	0.2	0.5	0.5	0.1	0.1	0.0	
0.936	0.009	0.004	0.1	0.1	0.1	0.1	0.2	0.1	0.0	
1.242	0.010	0.002	0.1	0.1	0.0	0.1	0.1	0.1	0.0	
1.382	0.002	0.002	0.0	0.0	-0.0	0.0	0.0	0.0	0.0	
Arid										
0.466	0.352	0.060	35.6	39.7	15.3	25.2	44.5	14.7	-0.3	
0.554	0.462	0.069	39.7	47.8	17.2	28.0	53.6	16.5	-0.5	
0.646	0.223	0.030	15.3	17.2	8.8	12.4	18.9	4.7	-0.3	
0.856	0.273	0.044	25.2	28.0	12.4	19.1	31.1	9.6	-0.3	
0.936	0.544	0.082	44.5	53.6	18.9	31.1	67.0	20.2	-0.4	
1.242	0.243	0.037	14.7	16.5	4.7	9.6	20.2	13.5	0.4	
1.382	0.005	0.003	-0.3	-0.5	-0.3	-0.3	-0.4	0.4	0.1	

Table 5: Thresholded surface class means, standard deviations, and covariance matrices for each of the MODIS reflectance bands selected for classification.

$\lambda$	$\mu$	$\sigma$	Brightness Temp. Covariance ( $\times 10^2$ )			
Ice Cloud						
3.79	297.5	8.23	6771.7	808.8	332.1	711.5
7.34	249.7	2.19	808.8	479.0	317.0	475.6
8.53	277.4	7.32	332.1	317.0	5356.4	5191.0
11.00	277.4	7.19	711.5	475.6	5191.0	5163.8
Water Cloud						
3.79	313.5	2.98	888.6	176.3	244.8	270.8
7.34	254.1	1.28	176.3	164.8	195.4	233.4
8.53	276.8	2.47	244.8	195.4	612.1	627.3
11.00	278.8	2.61	270.8	233.4	627.3	683.9
Vegetation						
3.79	312.6	3.47	1201.7	212.7	867.3	1000.8
7.34	256.4	1.36	212.7	185.1	213.2	273.4
8.53	299.6	3.14	867.3	213.2	983.6	1063.9
11.00	301.7	3.51	1000.8	273.4	1063.9	1229.4
Water						
3.79	291.1	0.97	94.4	56.1	87.1	76.3
7.34	254.5	1.03	56.1	106.4	79.5	71.0
8.53	285.9	1.12	87.1	79.5	126.1	117.3
11.00	288.2	1.09	76.3	71.0	117.3	119.8
Arid						
3.79	321.4	3.77	1418.6	350.3	-164.7	832.2
7.34	259.2	2.69	350.3	726.0	330.6	475.0
8.53	301.3	3.24	-164.7	330.6	1047.7	357.2
11.00	306.7	2.92	832.2	475.0	357.2	855.3

Figure 10: thresh brightness temp. statistics

### Thresholded surface class analysis

Figure 9 shows the standard deviation and mean spectral response of each of my surface classes, using all the bands in Table 2. The reflectance of ice clouds in the top image has the largest standard deviation of all surface classes due to the aforementioned presence of water-phase clouds and the wide range in cirrus optical depth. Nonetheless, it's clear that the slope of mean ice cloud reflectance is less affected by absorption lines at  $.856\mu m$ ,  $.936\mu m$ , and  $1.382\mu m$  due to the relative scarcity of water vapor above the cirrus clouds' altitude. Table 5 indicates that the reflectance curve of the vegetation class has a much lower standard deviation of around .03 in window bands. The hallmark jump in NIR reflectance over vegetation is readily apparent in its spectral response curve in Figure 9. The reflectance spectral response of water is most consistent, and characteristically peaks in the blue range decreasing steeply to almost zero into the NIR range. As their bright white color suggests, clouds are by far the most reflective class in the visible range. The relatively high reflectivity of water clouds in the  $1.629\mu m$  cloud phase band isn't well-represented by the thresholded samples because most of the cirrus clouds in my image are extremely thin, as mentioned in Section 3. I chose not to use the  $1.629\mu m$  band in classification because of these challenges, which means I will rely on infrared and  $1.37\mu m$  NIR absorption bands alone for cirrus identification.

## 6 K-means classification

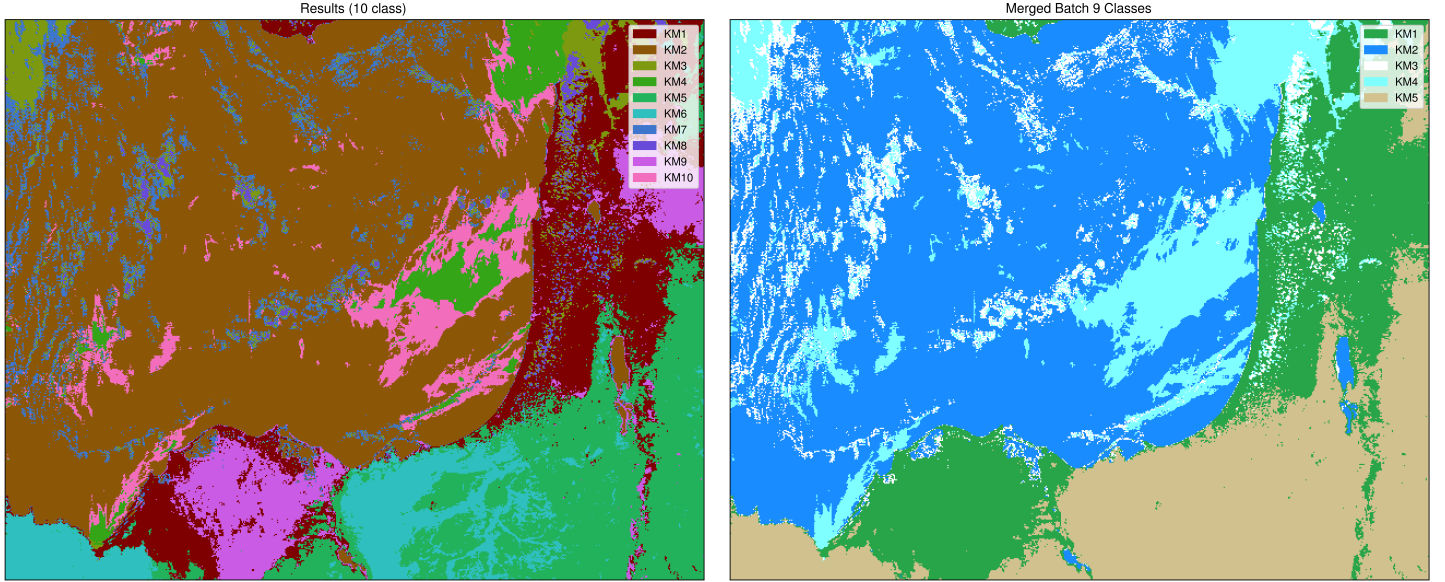


Figure 11: Final set of K-means results, which were trained on the 11 starred bands in Table 2. I determined that 10 classes was an appropriate number of categories to capture a variety of features without finding mean vectors that are too close together given the bands I selected. These 10 classes were subsequently manually merged to reflect the 5 surface classes I chose for analysis.

	KM1 (vegetation)	KM2 (water)	KM3 (water cloud)	KM4 (ice cloud)	KM5 (arid)
Pixel Count	57,991	149,596	20,064	37,428	62,601
Area (km <sup>2</sup> )	71,817	277,355	42,338	58,480	78,696

Figure 12: Area and quantity of K-means pixel classes.

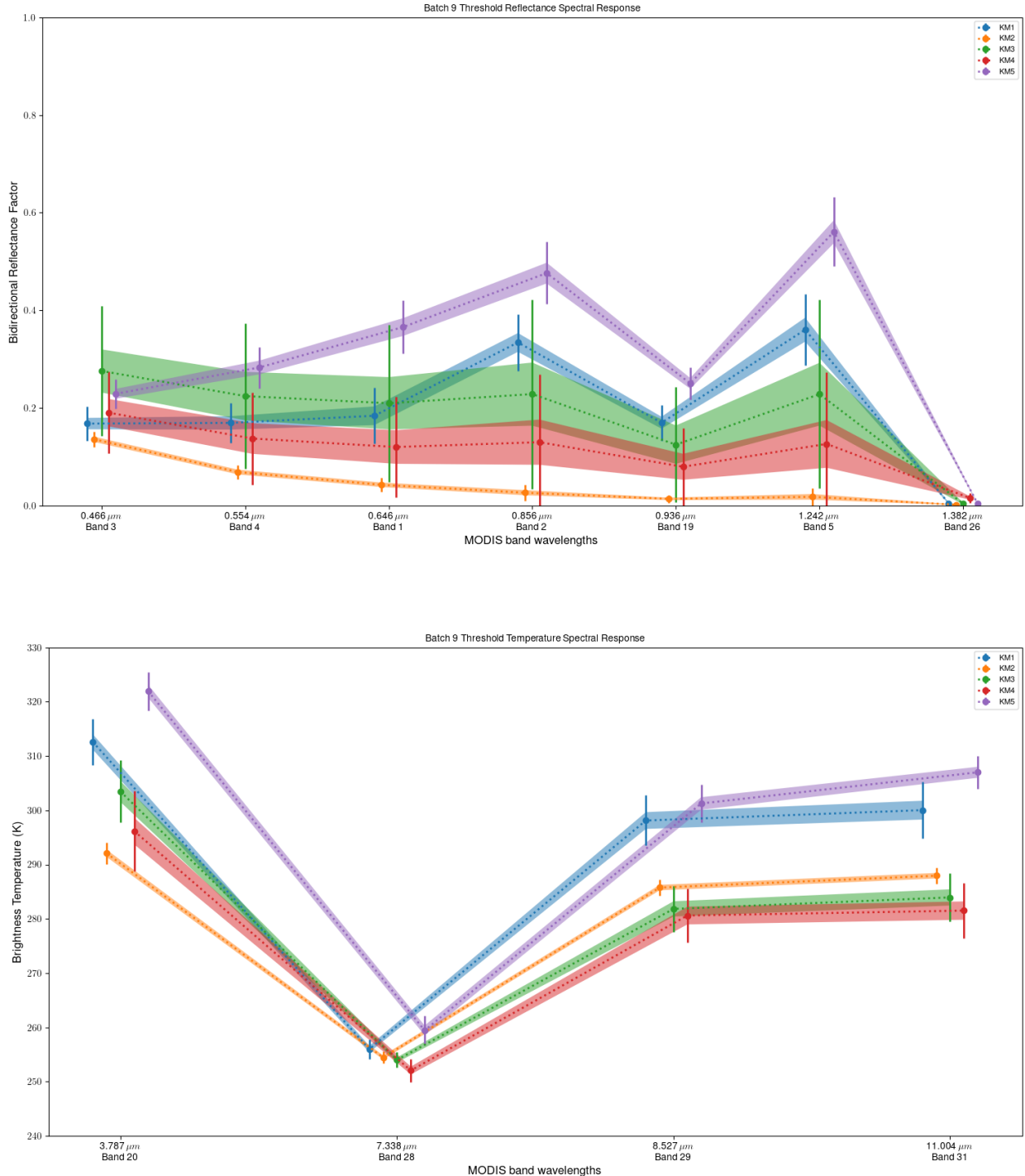


Figure 13:

$\lambda$	$\mu$	$\sigma$	Reflectance Covariance ( $\times 10^4$ )							
KM1										
0.466	0.168	0.035	12.3	13.4	15.3	11.1	5.7	14.8	0.5	
0.554	0.170	0.041	13.4	16.8	22.0	15.7	9.4	22.0	0.7	
0.646	0.184	0.057	15.3	22.0	32.7	20.4	14.1	31.3	1.2	
0.856	0.334	0.058	11.1	15.7	20.4	33.3	17.6	39.2	0.7	
0.936	0.170	0.036	5.7	9.4	14.1	17.6	13.3	22.8	1.0	
1.242	0.361	0.074	14.8	22.0	31.3	39.2	22.8	54.1	1.3	
1.382	0.005	0.005	0.5	0.7	1.2	0.7	1.0	1.3	0.3	
KM2										
0.466	0.043	0.014	1.9	2.1	1.8	1.9	2.3	1.0	0.0	
0.554	0.027	0.016	2.1	2.5	1.8	2.0	2.7	1.2	0.0	
0.646	0.136	0.016	1.8	1.8	2.6	1.9	1.9	0.8	-0.1	
0.856	0.069	0.015	1.9	2.0	1.9	2.1	2.2	0.9	0.0	
0.936	0.018	0.018	2.3	2.7	1.9	2.2	3.1	1.3	0.0	
1.242	0.014	0.008	1.0	1.2	0.8	0.9	1.3	0.6	0.0	
1.382	0.002	0.002	0.0	0.0	-0.1	0.0	0.0	0.0	0.1	
KM3										
0.466	0.210	0.161	257.8	308.1	210.7	238.6	301.9	185.3	5.3	
0.554	0.229	0.194	308.1	375.5	249.0	284.6	370.1	226.1	6.7	
0.646	0.276	0.133	210.7	249.0	175.6	195.9	243.7	149.3	4.0	
0.856	0.225	0.149	238.6	284.6	195.9	221.2	278.7	171.0	4.8	
0.936	0.228	0.193	301.9	370.1	243.7	278.7	372.0	223.3	6.7	
1.242	0.125	0.118	185.3	226.1	149.3	171.0	223.3	138.1	4.5	
1.382	0.004	0.006	5.3	6.7	4.0	4.8	6.7	4.5	0.3	
KM4										
0.466	0.120	0.103	106.5	138.2	82.6	96.6	143.1	78.3	-0.1	
0.554	0.130	0.139	138.2	192.6	101.1	123.8	201.5	109.2	0.7	
0.646	0.191	0.084	82.6	101.1	70.4	77.2	104.5	56.7	-0.8	
0.856	0.138	0.094	96.6	123.8	77.2	88.6	128.0	69.9	-0.3	
0.936	0.127	0.147	143.1	201.5	104.5	128.0	215.0	114.3	0.8	
1.242	0.080	0.080	78.3	109.2	56.7	69.9	114.3	63.4	1.2	
1.382	0.016	0.010	-0.1	0.7	-0.8	-0.3	0.8	1.2	0.9	
KM5										
0.466	0.366	0.055	29.8	33.7	13.9	22.0	34.6	10.5	-0.3	
0.554	0.476	0.064	33.7	40.6	15.9	24.9	42.0	11.5	-0.5	
0.646	0.229	0.030	13.9	15.9	9.2	12.0	15.9	3.8	-0.3	
0.856	0.283	0.042	22.0	24.9	12.0	17.8	25.1	7.5	-0.3	
0.936	0.561	0.071	34.6	42.0	15.9	25.1	49.8	12.8	-0.5	
1.242	0.251	0.033	10.5	11.5	3.8	7.5	12.8	10.9	0.4	
1.382	0.005	0.003	-0.3	-0.5	-0.3	-0.3	-0.5	0.4	0.1	

Table 6: km reflectance statistics

$\lambda$	$\mu$	$\sigma$	Brightness	Temp.	Covariance ( $\times 10^2$ )	
KM1						
3.79	312.6	4.23	1793.4	395.7	1422.1	1661.1
7.34	256.0	1.79	395.7	319.0	470.3	586.3
8.53	298.1	4.63	1422.1	470.3	2146.3	2363.0
11.00	300.0	5.20	1661.1	586.3	2363.0	2704.1
KM2						
3.79	292.1	2.01	404.0	60.5	94.8	83.7
7.34	254.5	1.12	60.5	126.4	114.8	107.6
8.53	285.8	1.51	94.8	114.8	228.1	223.0
11.00	287.9	1.53	83.7	107.6	223.0	233.9
KM3						
3.79	303.5	5.72	3276.2	110.1	-959.3	-1048.7
7.34	254.0	1.39	110.1	193.1	311.5	332.5
8.53	281.8	4.22	-959.3	311.5	1777.6	1873.9
11.00	284.0	4.48	-1048.7	332.5	1873.9	2009.4
KM4						
3.79	296.2	7.35	5405.7	478.3	-1124.8	-932.1
7.34	252.1	2.17	478.3	469.9	459.4	596.8
8.53	280.6	4.90	-1124.8	459.4	2404.9	2440.2
11.00	281.5	5.06	-932.1	596.8	2440.2	2563.5
KM5						
3.79	322.0	3.55	1257.1	272.8	-185.0	741.5
7.34	259.4	2.66	272.8	709.5	412.8	470.0
8.53	301.3	3.45	-185.0	412.8	1192.0	460.9
11.00	307.0	3.03	741.5	470.0	460.9	918.3

Table 7: km brightness temp. statistics

	Ice	Cloud	Water	Cloud	Vegetation	Water	Arid	Cons. Acc.
KM1	766		0		35940	0	8023	0.804
KM2	0		0		195	96348	79	0.997
KM3	518		2213		326	0	5	0.723
KM4	8736		12		0	382	0	0.957
KM5	74		2		153	0	60815	0.996
Prod. Acc.	0.865		0.994		0.982	0.996	0.882	

Table 8: km/thresh confusion matrix

## 7 Tables

	Ice Cloud	Water Cloud	Vegetation	Water	Arid
Pixel Count	393	369	397	399	399
Area (km <sup>2</sup> )	560	519	532	742	518

Figure 14: Area and quantity of samples chosen from thresholded pixel classes.

	Ice Cloud	Water Cloud	Vegetation	Water	Arid	Uncertain
Pixel Count	69620	5799	43344	125432	68670	14815
Area (km <sup>2</sup> )	124604	8654	55828	226847	85326	27429

Figure 15: Area and quantity of pixel classes from maximum-likelihood classification using samples chosen from thresholded classes.

	KM1	KM2	KM3	KM4	KM5
Pixel Count	398	400	396	397	397
Area (km <sup>2</sup> )	485	747	846	609	497

Figure 16: Area and quantity of samples chosen from K-means pixel classes.

	KM1	KM2	KM3	KM4	KM5	Uncertain
Pixel Count	58435	155717	24430	22898	61084	5116
Area (km <sup>2</sup> )	71943	287288	49023	35537	77089	7806

Figure 17: Area and quantity of pixel classes from maximum-likelihood classification using K-means samples chosen from K-means classes.

$\lambda$	$\mu$	$\sigma$	Reflectance Covariance ( $\times 10^4$ )						
Ice Cloud									
0.466	0.210	0.100	99.5	106.9	113.7	126.1	79.8	122.4	0.0
0.554	0.172	0.112	106.9	124.6	138.7	168.7	103.6	168.5	0.3
0.646	0.164	0.126	113.7	138.7	158.5	199.1	120.8	202.2	0.4
0.856	0.201	0.167	126.1	168.7	199.1	281.1	167.1	295.0	1.4
0.936	0.131	0.101	79.8	103.6	120.8	167.1	101.4	174.4	1.1
1.242	0.203	0.179	122.4	168.5	202.2	295.0	174.4	321.5	1.5
1.382	0.029	0.008	0.0	0.3	0.4	1.4	1.1	1.5	0.6
Water Cloud									
0.466	0.564	0.094	89.2	82.8	87.2	87.3	66.0	47.4	-0.4
0.554	0.645	0.092	82.8	85.4	78.3	80.7	72.0	52.2	0.5
0.646	0.570	0.094	87.2	78.3	89.1	86.8	61.0	42.3	-1.0
0.856	0.553	0.093	87.3	80.7	86.8	86.2	63.9	45.7	-0.5
0.936	0.635	0.085	66.0	72.0	61.0	63.9	72.6	46.0	0.9
1.242	0.372	0.062	47.4	52.2	42.3	45.7	46.0	38.3	1.4
1.382	0.009	0.006	-0.4	0.5	-1.0	-0.5	0.9	1.4	0.3
Vegetation									
0.466	0.152	0.033	10.8	8.4	4.8	7.0	15.1	5.4	0.3
0.554	0.314	0.056	8.4	31.2	4.9	7.7	33.6	13.5	0.0
0.646	0.152	0.021	4.8	4.9	4.6	4.6	7.4	0.9	-0.0
0.856	0.147	0.024	7.0	7.7	4.6	5.7	11.5	3.3	0.1
0.936	0.330	0.067	15.1	33.6	7.4	11.5	44.7	16.2	0.3
1.242	0.153	0.030	5.4	13.5	0.9	3.3	16.2	8.7	0.3
1.382	0.003	0.003	0.3	0.0	-0.0	0.1	0.3	0.3	0.1
Water									
0.466	0.036	0.004	0.2	0.1	0.3	0.3	0.1	0.1	0.0
0.554	0.018	0.004	0.1	0.1	0.2	0.1	0.1	0.1	0.0
0.646	0.131	0.010	0.3	0.2	1.1	0.5	0.1	0.0	-0.0
0.856	0.062	0.007	0.3	0.1	0.5	0.5	0.1	0.1	0.0
0.936	0.009	0.004	0.1	0.1	0.1	0.1	0.1	0.1	0.0
1.242	0.010	0.002	0.1	0.1	0.0	0.1	0.1	0.0	0.0
1.382	0.002	0.002	0.0	0.0	-0.0	0.0	0.0	0.0	0.0
Arid									
0.466	0.349	0.061	37.3	41.6	16.5	26.5	47.5	14.6	-0.4
0.554	0.459	0.071	41.6	49.9	18.5	29.6	56.9	16.4	-0.6
0.646	0.222	0.031	16.5	18.5	9.4	13.1	20.8	4.6	-0.3
0.856	0.271	0.045	26.5	29.6	13.1	20.1	33.4	9.7	-0.3
0.936	0.539	0.085	47.5	56.9	20.8	33.4	71.6	20.1	-0.6
1.242	0.240	0.037	14.6	16.4	4.6	9.7	20.1	13.7	0.4
1.382	0.005	0.003	-0.4	-0.6	-0.3	-0.3	-0.6	0.4	0.1

Figure 18: samples thresh reflectance statistics

$\lambda$	$\mu$	$\sigma$	Brightness Temp. Covariance ( $\times 10^2$ )			
Ice Cloud						
3.79	297.0	8.04	6484.6	688.3	18.0	410.4
7.34	249.6	2.09	688.3	438.8	181.6	358.7
8.53	277.3	6.86	18.0	181.6	4712.9	4547.5
11.00	277.4	6.72	410.4	358.7	4547.5	4533.0
Water Cloud						
3.79	313.6	3.07	942.3	216.7	341.8	380.8
7.34	254.2	1.35	216.7	183.3	242.5	280.3
8.53	276.9	2.62	341.8	242.5	687.8	714.4
11.00	278.8	2.79	380.8	280.3	714.4	781.0
Vegetation						
3.79	312.6	3.47	1210.5	273.0	844.8	1020.5
7.34	256.4	1.44	273.0	209.3	253.8	336.3
8.53	299.5	3.04	844.8	253.8	925.8	1022.5
11.00	301.7	3.50	1020.5	336.3	1022.5	1226.4
Water						
3.79	291.1	0.97	94.3	60.7	87.6	77.9
7.34	254.5	1.05	60.7	110.1	84.9	77.8
8.53	286.0	1.12	87.6	84.9	126.2	118.8
11.00	288.2	1.11	77.9	77.8	118.8	123.0
Arid						
3.79	321.1	3.80	1450.6	389.8	-108.0	836.4
7.34	258.9	2.81	389.8	792.3	366.1	493.1
8.53	301.6	3.35	-108.0	366.1	1123.1	424.3
11.00	306.6	2.93	836.4	493.1	424.3	859.3

Figure 19: samples thresh brightness temp. statistics

$\lambda$	$\mu$	$\sigma$	Reflectance Covariance ( $\times 10^4$ )						
Ice Cloud									
0.466	0.187	0.059	34.3	37.7	40.7	50.9	29.4	54.3	0.3
0.554	0.132	0.069	37.7	47.3	54.2	75.0	43.8	81.4	1.2
0.646	0.115	0.080	40.7	54.2	63.9	91.2	53.5	100.0	1.8
0.856	0.125	0.119	50.9	75.0	91.2	141.8	82.9	156.7	3.3
0.936	0.072	0.070	29.4	43.8	53.5	82.9	49.7	91.5	2.7
1.242	0.126	0.132	54.3	81.4	100.0	156.7	91.5	175.2	3.5
1.382	0.009	0.010	0.3	1.2	1.8	3.3	2.7	3.5	1.0
Water Cloud									
0.466	0.442	0.121	147.5	149.5	134.3	141.1	131.9	91.8	1.8
0.554	0.522	0.130	149.5	168.8	129.2	141.6	154.0	107.3	3.3
0.646	0.461	0.112	134.3	129.2	126.4	129.6	110.9	77.1	0.8
0.856	0.438	0.116	141.1	141.6	129.6	135.4	123.9	86.4	1.5
0.936	0.528	0.122	131.9	154.0	110.9	123.9	148.6	99.8	3.6
1.242	0.297	0.085	91.8	107.3	77.1	86.4	99.8	72.4	3.0
1.382	0.008	0.006	1.8	3.3	0.8	1.5	3.6	3.0	0.4
Vegetation									
0.466	0.159	0.039	15.0	11.3	6.7	9.9	18.8	6.9	0.5
0.554	0.321	0.056	11.3	31.2	5.8	9.2	35.3	14.6	0.2
0.646	0.156	0.024	6.7	5.8	5.6	5.9	8.6	1.6	0.1
0.856	0.153	0.027	9.9	9.2	5.9	7.6	13.6	4.4	0.2
0.936	0.340	0.069	18.8	35.3	8.6	13.6	46.9	18.2	0.6
1.242	0.158	0.032	6.9	14.6	1.6	4.4	18.2	10.0	0.5
1.382	0.003	0.004	0.5	0.2	0.1	0.2	0.6	0.5	0.1
Water									
0.466	0.038	0.006	0.3	0.3	0.4	0.4	0.3	0.2	0.0
0.554	0.021	0.006	0.3	0.3	0.3	0.3	0.4	0.2	0.1
0.646	0.131	0.011	0.4	0.3	1.2	0.6	0.2	0.1	-0.0
0.856	0.064	0.007	0.4	0.3	0.6	0.5	0.3	0.1	0.0
0.936	0.012	0.006	0.3	0.4	0.2	0.3	0.4	0.2	0.1
1.242	0.012	0.004	0.2	0.2	0.1	0.1	0.2	0.1	0.1
1.382	0.003	0.003	0.0	0.1	-0.0	0.0	0.1	0.1	0.1
Arid									
0.466	0.355	0.061	37.1	41.9	17.0	27.2	45.9	15.0	-0.4
0.554	0.464	0.071	41.9	49.8	19.2	30.6	54.8	16.8	-0.5
0.646	0.224	0.031	17.0	19.2	9.8	13.9	20.8	5.4	-0.3
0.856	0.275	0.046	27.2	30.6	13.9	21.2	33.3	10.5	-0.4
0.936	0.546	0.082	45.9	54.8	20.8	33.3	66.9	19.8	-0.5
1.242	0.245	0.036	15.0	16.8	5.4	10.5	19.8	13.3	0.3
1.382	0.005	0.003	-0.4	-0.5	-0.3	-0.4	-0.5	0.3	0.1

Figure 20: mlc thresh reflectance statistics

$\lambda$	$\mu$	$\sigma$	Brightness Temp. Covariance ( $\times 10^2$ )			
Ice Cloud						
3.79	297.7	6.38	4068.9	332.0	262.8	305.2
7.34	253.1	2.04	332.0	416.3	501.6	645.5
8.53	282.8	4.88	262.8	501.6	2384.7	2467.6
11.00	284.2	5.15	305.2	645.5	2467.6	2652.6
Water Cloud						
3.79	312.6	2.79	775.9	150.9	200.9	179.8
7.34	254.2	1.29	150.9	166.1	271.4	292.2
8.53	278.8	3.38	200.9	271.4	1143.4	1106.7
11.00	280.6	3.35	179.8	292.2	1106.7	1119.1
Vegetation						
3.79	312.0	4.04	1634.5	320.6	1293.6	1486.3
7.34	256.1	1.38	320.6	189.6	344.3	408.9
8.53	298.7	3.88	1293.6	344.3	1502.7	1671.5
11.00	300.6	4.39	1486.3	408.9	1671.5	1926.1
Water						
3.79	291.3	1.09	117.8	47.3	74.1	57.0
7.34	254.4	1.07	47.3	114.9	90.8	87.3
8.53	285.8	1.20	74.1	90.8	144.7	145.0
11.00	287.9	1.28	57.0	87.3	145.0	163.5
Arid						
3.79	321.5	3.72	1386.7	355.0	-158.1	827.1
7.34	259.2	2.72	355.0	739.6	343.6	478.9
8.53	301.4	3.28	-158.1	343.6	1078.8	377.2
11.00	306.8	2.94	827.1	478.9	377.2	863.8

Figure 21: mlc thresh brightness temp. statistics

	Ice Cloud	Water Cloud	Vegetation	Water	Arid	Uncertain	Cons. Acc.
MLC Ice Cloud	372	4	0	0	0	17	0.947
MLC Water Cloud	2	361	0	0	0	6	0.978
MLC Vegetation	1	0	387	0	5	4	0.975
MLC Water	0	0	0	395	0	4	0.990
MLC Arid	0	0	9	0	385	5	0.965
Prod. Acc.	0.992	0.989	0.977	1.000	0.987		

Figure 22: samples thresh/mlc thresh confusion matrix

$\lambda$	$\mu$	$\sigma$	Reflectance Covariance ( $\times 10^4$ )							
0.466	0.145	0.121	147.0	200.1	83.0	115.5	204.5	109.3	4.1	
0.554	0.171	0.174	200.1	302.4	107.4	154.8	316.6	163.6	5.7	
0.646	0.191	0.078	83.0	107.4	60.1	70.5	104.4	59.7	2.1	
0.856	0.159	0.097	115.5	154.8	70.5	94.3	155.0	85.0	3.2	
0.936	0.170	0.187	204.5	316.6	104.4	155.0	348.6	169.9	5.8	
1.242	0.088	0.095	109.3	163.6	59.7	85.0	169.9	91.0	3.6	
1.382	0.005	0.008	4.1	5.7	2.1	3.2	5.8	3.6	0.6	
$\lambda$	$\mu$	$\sigma$	Brightness Temp. Covariance ( $\times 10^2$ )							
3.79	301.3	9.38	8802.7	881.8	3530.7	3898.1				
7.34	254.8	2.59	881.8	673.2	1113.9	1227.8				
8.53	288.2	6.16	3530.7	1113.9	3790.0	4043.4				
11.00	290.6	6.69	3898.1	1227.8	4043.4	4480.2				

Figure 23: mlc thresh Uncertain reflectance and brightness temp. statistics

$\lambda$	$\mu$	$\sigma$	Reflectance Covariance ( $\times 10^4$ )						
KM1									
0.466	0.168	0.035	12.2	13.5	15.3	11.1	6.2	15.0	0.6
0.554	0.169	0.041	13.5	17.0	21.8	15.5	9.9	21.9	0.9
0.646	0.183	0.057	15.3	21.8	32.2	20.5	14.8	31.5	1.6
0.856	0.331	0.059	11.1	15.5	20.5	34.8	19.4	41.1	1.1
0.936	0.168	0.038	6.2	9.9	14.8	19.4	14.5	25.1	1.2
1.242	0.356	0.075	15.0	21.9	31.5	41.1	25.1	56.1	1.8
1.382	0.005	0.005	0.6	0.9	1.6	1.1	1.2	1.8	0.3
KM2									
0.466	0.043	0.013	1.8	2.1	1.7	1.8	2.1	1.0	0.0
0.554	0.027	0.016	2.1	2.4	1.7	2.0	2.5	1.2	0.0
0.646	0.136	0.016	1.7	1.7	2.4	1.8	1.7	0.8	-0.0
0.856	0.069	0.014	1.8	2.0	1.8	1.9	2.0	0.9	0.0
0.936	0.018	0.016	2.1	2.5	1.7	2.0	2.7	1.2	0.1
1.242	0.014	0.008	1.0	1.2	0.8	0.9	1.2	0.6	0.1
1.382	0.002	0.002	0.0	0.0	-0.0	0.0	0.1	0.1	0.1
KM3									
0.466	0.223	0.169	285.6	341.1	232.2	264.5	326.0	208.9	7.0
0.554	0.243	0.203	341.1	414.5	275.0	315.6	400.5	254.1	8.6
0.646	0.287	0.138	232.2	275.0	192.0	215.8	262.9	167.8	5.3
0.856	0.237	0.156	264.5	315.6	215.8	245.4	301.4	193.1	6.4
0.936	0.241	0.200	326.0	400.5	262.9	301.4	400.4	245.6	8.2
1.242	0.134	0.125	208.9	254.1	167.8	193.1	245.6	157.8	5.7
1.382	0.005	0.006	7.0	8.6	5.3	6.4	8.2	5.7	0.4
KM4									
0.466	0.123	0.103	107.0	139.1	80.3	96.2	137.9	78.5	-0.4
0.554	0.134	0.140	139.1	195.4	98.3	123.4	197.9	111.2	0.6
0.646	0.191	0.082	80.3	98.3	66.7	74.4	97.7	54.4	-1.2
0.856	0.140	0.093	96.2	123.4	74.4	87.4	122.3	69.2	-0.6
0.936	0.129	0.144	137.9	197.9	97.7	122.3	207.7	112.5	0.8
1.242	0.082	0.080	78.5	111.2	54.4	69.2	112.5	64.7	1.1
1.382	0.016	0.010	-0.4	0.6	-1.2	-0.6	0.8	1.1	1.0
KM5									
0.466	0.369	0.057	32.1	36.7	14.8	23.6	36.3	11.7	-0.3
0.554	0.480	0.067	36.7	44.4	16.9	26.9	44.4	13.0	-0.5
0.646	0.231	0.030	14.8	16.9	9.2	12.5	16.3	4.1	-0.2
0.856	0.286	0.043	23.6	26.9	12.5	18.8	26.2	8.1	-0.3
0.936	0.565	0.071	36.3	44.4	16.3	26.2	50.4	13.4	-0.6
1.242	0.253	0.035	11.7	13.0	4.1	8.1	13.4	12.0	0.4
1.382	0.005	0.004	-0.3	-0.5	-0.2	-0.3	-0.6	0.4	0.1

Figure 24: samples km reflectance statistics

$\lambda$	$\mu$	$\sigma$	Brightness Temp. Covariance ( $\times 10^2$ )			
KM1						
3.79	312.7	4.10	1685.3	314.2	1303.2	1523.8
7.34	256.0	1.73	314.2	300.9	410.4	525.2
8.53	298.1	4.64	1303.2	410.4	2158.9	2360.5
11.00	300.0	5.18	1523.8	525.2	2360.5	2689.2
KM2						
3.79	292.0	2.01	406.1	58.5	89.6	76.4
7.34	254.5	1.06	58.5	112.2	96.9	89.4
8.53	285.7	1.41	89.6	96.9	198.8	194.2
11.00	287.8	1.43	76.4	89.4	194.2	205.7
KM3						
3.79	303.7	5.85	3428.4	103.2	-941.2	-1023.6
7.34	253.9	1.42	103.2	202.4	354.6	382.2
8.53	281.4	4.28	-941.2	354.6	1836.7	1961.1
11.00	283.6	4.60	-1023.6	382.2	1961.1	2123.0
KM4						
3.79	296.2	7.20	5201.2	533.0	-853.1	-646.2
7.34	252.0	2.21	533.0	489.8	455.0	599.3
8.53	280.6	4.49	-853.1	455.0	2019.8	2082.2
11.00	281.5	4.72	-646.2	599.3	2082.2	2234.2
KM5						
3.79	322.0	3.63	1321.8	270.2	-203.2	767.7
7.34	259.5	2.79	270.2	782.2	489.4	516.5
8.53	301.0	3.56	-203.2	489.4	1270.3	480.4
11.00	306.9	3.08	767.7	516.5	480.4	953.2

Figure 25: samples km brightness temp. statistics

$\lambda$	$\mu$	$\sigma$	Reflectance Covariance ( $\times 10^4$ )						
KM1									
0.466	0.167	0.033	10.7	12.0	14.4	10.9	5.6	15.0	0.5
0.554	0.169	0.040	12.0	15.9	21.7	16.4	9.8	23.3	0.8
0.646	0.184	0.058	14.4	21.7	33.4	22.2	15.2	34.1	1.3
0.856	0.335	0.059	10.9	16.4	22.2	34.8	18.5	41.7	0.7
0.936	0.170	0.037	5.6	9.8	15.2	18.5	13.7	24.2	1.0
1.242	0.362	0.076	15.0	23.3	34.1	41.7	24.2	57.2	1.3
1.382	0.005	0.005	0.5	0.8	1.3	0.7	1.0	1.3	0.3
KM2									
0.466	0.042	0.013	1.6	1.7	1.6	1.6	1.9	0.8	0.0
0.554	0.026	0.014	1.7	2.0	1.6	1.6	2.1	1.0	0.1
0.646	0.136	0.016	1.6	1.6	2.5	1.8	1.7	0.7	-0.1
0.856	0.068	0.013	1.6	1.6	1.8	1.7	1.8	0.8	0.0
0.936	0.018	0.015	1.9	2.1	1.7	1.8	2.4	1.1	0.1
1.242	0.014	0.007	0.8	1.0	0.7	0.8	1.1	0.5	0.1
1.382	0.003	0.003	0.0	0.1	-0.1	0.0	0.1	0.1	0.1
KM3									
0.466	0.206	0.147	216.6	262.0	180.4	200.1	263.1	154.1	3.8
0.554	0.223	0.179	262.0	321.7	216.0	241.6	324.2	190.0	4.9
0.646	0.272	0.124	180.4	216.0	152.9	167.1	216.4	126.3	2.9
0.856	0.221	0.136	200.1	241.6	167.1	185.1	242.2	141.9	3.4
0.936	0.224	0.182	263.1	324.2	216.4	242.2	331.2	191.9	5.0
1.242	0.120	0.107	154.1	190.0	126.3	141.9	191.9	113.8	3.2
1.382	0.003	0.005	3.8	4.9	2.9	3.4	5.0	3.2	0.2
KM4									
0.466	0.120	0.089	79.9	114.6	58.7	71.7	121.9	66.7	-0.1
0.554	0.132	0.132	114.6	175.4	78.7	101.5	187.5	101.2	0.1
0.646	0.190	0.070	58.7	78.7	48.8	54.6	83.8	45.9	-0.5
0.856	0.138	0.081	71.7	101.5	54.6	65.2	108.0	59.0	-0.2
0.936	0.131	0.142	121.9	187.5	83.8	108.0	202.1	108.0	-0.1
1.242	0.084	0.077	66.7	101.2	45.9	59.0	108.0	59.3	0.6
1.382	0.018	0.009	-0.1	0.1	-0.5	-0.2	-0.1	0.6	0.9
KM5									
0.466	0.367	0.054	29.6	34.7	13.9	22.0	35.2	10.4	-0.4
0.554	0.476	0.065	34.7	42.3	16.3	25.6	43.6	11.9	-0.6
0.646	0.229	0.029	13.9	16.3	8.5	11.7	16.4	3.7	-0.3
0.856	0.283	0.042	22.0	25.6	11.7	17.6	25.8	7.4	-0.4
0.936	0.562	0.071	35.2	43.6	16.4	25.8	51.1	13.0	-0.5
1.242	0.251	0.033	10.4	11.9	3.7	7.4	13.0	11.0	0.4
1.382	0.005	0.003	-0.4	-0.6	-0.3	-0.4	-0.5	0.4	0.1

Figure 26: mlc km reflectance statistics

$\lambda$	$\mu$	$\sigma$	Brightness Temp. Covariance ( $\times 10^2$ )			
KM1						
3.79	312.7	4.55	2073.3	447.9	1684.4	1947.3
7.34	255.9	1.76	447.9	308.2	541.8	657.6
8.53	298.2	4.81	1684.4	541.8	2317.0	2579.9
11.00	300.1	5.44	1947.3	657.6	2579.9	2957.5
KM2						
3.79	291.9	1.68	281.2	26.2	16.1	2.0
7.34	254.3	1.12	26.2	126.0	104.7	102.4
8.53	285.5	1.33	16.1	104.7	176.4	178.0
11.00	287.6	1.42	2.0	102.4	178.0	201.0
KM3						
3.79	303.6	5.89	3464.0	22.8	-1246.9	-1344.6
7.34	254.3	1.32	22.8	173.9	311.9	317.7
8.53	282.5	4.08	-1246.9	311.9	1663.4	1712.0
11.00	284.7	4.23	-1344.6	317.7	1712.0	1787.1
KM4						
3.79	296.6	7.48	5598.9	742.4	-849.9	-645.4
7.34	251.6	2.27	742.4	514.4	530.5	680.7
8.53	279.6	5.29	-849.9	530.5	2798.8	2840.6
11.00	280.2	5.44	-645.4	680.7	2840.6	2964.9
KM5						
3.79	321.9	3.61	1302.8	265.5	-195.0	753.4
7.34	259.5	2.65	265.5	704.8	417.3	449.5
8.53	301.2	3.30	-195.0	417.3	1091.7	356.6
11.00	307.0	2.84	753.4	449.5	356.6	809.4

Figure 27: mlc km brightness temp. statistics

	KM1	KM2	KM3	KM4	KM5	Uncertain	Cons.	Acc.
MLC1	375	0	2	6	9	6	0.942	
MLC2	0	384	13	1	0	2	0.960	
MLC3	6	16	337	23	0	14	0.851	
MLC4	6	104	48	219	0	20	0.552	
MLC5	11	0	0	0	383	3	0.965	
Prod. Acc.	0.942	0.762	0.843	0.880	0.977			

Figure 28: samples km/mlc km confusion matrix

$\lambda$	$\mu$	$\sigma$	Reflectance Covariance ( $\times 10^4$ )						
0.466	0.235	0.168	282.5	334.6	210.9	235.9	318.1	201.4	7.8
0.554	0.277	0.210	334.6	439.3	235.1	270.2	433.1	259.2	11.8
0.646	0.244	0.137	210.9	235.1	187.2	191.6	214.0	148.8	7.0
0.856	0.236	0.144	235.9	270.2	191.6	206.6	249.6	165.6	6.6
0.936	0.272	0.216	318.1	433.1	214.0	249.6	467.5	254.2	12.2
1.242	0.157	0.127	201.4	259.2	148.8	165.6	254.2	161.3	9.1
1.382	0.014	0.015	7.8	11.8	7.0	6.6	12.2	9.1	2.2
$\lambda$	$\mu$	$\sigma$	Brightness Temp. Covariance ( $\times 10^2$ )						
3.79	304.2	10.11	10215.1	1242.3	4219.0	5408.5			
7.34	254.3	4.13	1242.3	1706.9	3105.3	3723.4			
8.53	286.3	11.10	4219.0	3105.3	12328.1	13482.3			
11.00	288.5	12.30	5408.5	3723.4	13482.3	15132.9			

Figure 29: mlc km Uncertain reflectance and brightness temp. statistics

## References

- [1] Flasse and Ceccato, “A contextual algorithm for avhrr fire detection,” *International Journal of Remote Sensing*, vol. 17, 1996.
- [2] “Next generation satellite rgb dust imagery leads to operational changes at nws albuquerque,” *J. Operational Meteor.*, vol. 4.
- [3] J. Torres, S. Lindstrom, and A. Heidinger, “Goes-r abi day cloud type rgb quick guide,” November 2021.
- [4] J. Li, T. Schmit, X. Jin, and G. Martin, “Goes-r advanced baseline imager algorithm theoretical basis document for legacy atmospheric moisture profile,” July.
- [5] Platnick, Meyer, and King, “Cloud optical properties user’s guide for c6 & c6.1,” 7 2018.
- [6] A. V. D. Griend and M. Owe, “On the relationship between thermal emissivity and the normalized difference vegetation index for natural surfaces,” *International Journal of Remote Sensing*, vol. 14, October.
- [7] S. Mumford, ed., *Compact World Atlas*. Penguin Random House, 7 ed., 2001.
- [8] S. Mineo and G. Pappalardo, “Rock emissivity measurement for infrared thermography engineering geological applications,” *Applied Sciences*, April 2021.
- [9] B. Shimron, A. Eyal, and B. Y., “Sinai geological map. aeromagnetic map,”